

Purdue University  
**Purdue e-Pubs**

---

CTRC Research Publications

Cooling Technologies Research Center

---

2021

## Quantifying the pathways of latent heat dissipation during droplet freezing on cooled substrates

J. E. Castillo  
*Purdue University*

Y. Huang  
*Purdue University*

Z. Pan  
*Purdue University*

J. A. Weibel  
*Purdue University, [jaweibel@purdue.edu](mailto:jaweibel@purdue.edu)*

Follow this and additional works at: <https://docs.lib.purdue.edu/coolingpubs>

---

Castillo, J. E.; Huang, Y.; Pan, Z.; and Weibel, J. A., "Quantifying the pathways of latent heat dissipation during droplet freezing on cooled substrates" (2021). *CTRC Research Publications*. Paper 370.  
<https://docs.lib.purdue.edu/coolingpubs/370>

This document has been made available through Purdue e-Pubs, a service of the Purdue University Libraries.  
Please contact [epubs@purdue.edu](mailto:epubs@purdue.edu) for additional information.

# Quantifying the Pathways of Latent Heat Dissipation during Droplet Freezing on Cooled Substrates

Julian E. Castillo<sup>1</sup>, Yanbo Huang<sup>2</sup>, Zhenhai Pan<sup>2</sup>, and Justin A. Weibel<sup>1,\*</sup>

<sup>1</sup>School of Mechanical Engineering, Purdue University, West Lafayette IN 47907 USA.

<sup>2</sup>School of Mechanical Engineering, Shanghai Jiao Tong University, Shanghai, China.

\* Corresponding author.

E-mail addresses: [castil19@purdue.edu](mailto:castil19@purdue.edu) (Julian E. Castillo), [hyb728@sjtu.edu.cn](mailto:hyb728@sjtu.edu.cn) (Yanbo Huang)  
[panzh@sjtu.edu.cn](mailto:panzh@sjtu.edu.cn) (Zhenhai Pan), and [jaweibel@purdue.edu](mailto:jaweibel@purdue.edu) (Justin A. Weibel)

## Abstract

When a liquid droplet freezes on a cooled substrate, the portion of latent heat released by ice formation that is not immediately absorbed by the supercooled liquid droplet is transferred to the solid substrate below the droplet and the surrounding air. It is important to quantify heat dissipation through these two pathways because they govern the propagation of frost between multiple droplets. In this paper, infrared (IR) thermography measurements of the surface of a freezing droplet are used to quantify the fraction of latent heat released to the substrate and the ambient air. These IR measurements also show that the crystallization dynamics are related to the size of the droplet, as the freezing front moves slower in larger droplets. Numerical simulations of the solidification process are performed using the IR temperature data at the contact line of the droplet as a boundary condition. These simulations, which have good agreement with experimentally measured freezing times, reveal that the heat transferred to the substrate through the base contact area of the droplet is best described by a time-dependent temperature boundary condition, contrary to the constant values of base temperature and rates of heat transfer assumed in previous numerical simulations reported in the literature. In further contrast to the highly simplified descriptions of the interaction between a droplet and its surrounding used in previous models, the model developed in the current work accounts for heat conduction, convection, and evaporative cooling at the droplet-air interface. The simulation results indicate that only a small fraction of heat is lost through the droplet-air interface via conduction and evaporative cooling. The heat transfer rate to the substrate of the droplet is shown to be at least one order of magnitude greater than the heat transferred to the ambient air.

Keywords: droplet freezing; infrared thermography; water vapor distribution; recalescence; solidification

## Nomenclature

$A$	area ( $\text{m}^2$ )
$C$	vapor molar concentration ( $\text{mol} / \text{m}^3$ )
$c_p$	heat capacity ( $\text{J} / \text{kg K}$ )
$D$	diffusion coefficient in air ( $\text{m}^2 / \text{s}$ )
$E_{mush}$	mushy zone constant ( $\text{kg m}^3 / \text{s}$ )
$h_s$	sensible enthalpy ( $\text{J} / \text{kg}$ )
$h_{fg}$	latent heat of evaporation ( $\text{J} / \text{kg}$ )
$h_{fs}$	latent heat of fusion ( $\text{J} / \text{kg}$ )
$H$	total latent heat ( $\text{J} / \text{kg}$ )
$L$	latent heat for solidification ( $\text{J} / \text{kg}$ )
$k$	thermal conductivity ( $\text{W} / \text{m K}$ )
$M$	molecular weight ( $\text{kg} / \text{mol}$ )
$m''$	mass flux ( $\text{kg} / \text{m}^2 \text{s}$ )
$\vec{n}$	unit vector pointing normal to the droplet interface
$p$	pressure ( $\text{N} / \text{m}^2$ )
$R$	universal gas constant ( $\text{J} / \text{mol K}$ )
$s$	length along the arc of the droplet-gas interface ( $\text{m}$ )
$S_m$	mass source term ( $\text{kg} / \text{m}^3 \text{s}$ )
$S_h$	energy source term ( $\text{W} / \text{m}^3$ )
$S_p$	momentum sink term ( $\text{kg}/\text{m}^2 \text{s}$ )
$t$	time ( $\text{s}$ )
$T$	temperature ( $^{\circ}\text{C}$ )
$v$	droplet volume ( $\text{m}^3$ )
$\vec{V}$	fluid flow velocity ( $\text{m} / \text{s}$ )
$q$	heat transfer rate ( $\text{W}$ )

$q''$  heat flux (W/m<sup>2</sup>)

$x$  ice fraction

### **Greek**

$\alpha$  thermal diffusivity (m<sup>2</sup> / s)

$\beta$  liquid fraction

$\delta$  thickness of hydrodynamic boundary layer (m)

$\varepsilon$  constant

$\Gamma$  diffusivity coefficient (kg/ m s)

$\mu$  dynamic viscosity (N s/ m<sup>2</sup>)

$\rho$  density (kg / m<sup>3</sup>)

$\omega$  fraction of water-air mixture

$\xi$  any thermophysical property

### **Subscripts**

1 phase 1

2 phase 2

$\infty$  far field

*air* air

*atm* at atmospheric conditions

*c* the contact area between droplet and substrate

*cell* computational cell at the droplet-gas interface

*e<sub>q</sub>* at the equilibrium freezing temperature (0 °C for water)

*exp* experiment

*g* gas (vapor/air mixture)

*l* liquid

*liq* at liquidus condition

*lv* liquid-gas interface

*n* component in direction normal to the liquid-gas interface

*v* vapor

*p* porous-like media

*s* solid substrate

*sat* saturated  
*sol* at solidus condition  
*ref* reference  
*rec* recalescence  
*water* water

## 1.0. Introduction

Ice accumulation on the surfaces of aircraft, wind turbine blades, heat exchangers, transmission lines, and other infrastructure can compromise safety, efficiency, and cost of operation [1–5]. Compared to the active removal of ice by heating or mechanical means, passive prevention of the accumulation of ice is preferred to lower cost and energy use [6]. A commonly used passive method is to spread hygroscopic substances such as salts and glycols on surfaces, which delay ice formation but still have high operational costs and bring long-term environmental concerns [7]. A promising alternative is to engineer surfaces that delay the onset of freezing [8–10] and limit the propagation of frost once freezing has been initiated [11,12]. Surfaces with high hydrophobicity have been demonstrated [13,14] to delay nucleation of ice within condensate droplets by limiting the heat transfer at the droplet-substrate interface. Chemically patterned surfaces have also been designed to delay the propagation of frost by limiting the heat and mass transfer to nearby supercooled liquid droplets. Scalable methods to engineer hydrophobic surfaces are highly desired and have been demonstrated to improve system level efficiency by delaying the accumulation of frost [15,16]. Quantitative descriptions of the pathways of heat and mass transfer from a freezing droplet to its surroundings are fundamental to understanding the mechanisms governing inter-droplet freezing as well as to the engineering of surfaces that can passively prevent the accumulation of ice.

Liquid droplets resting on a substrate cooled below the equilibrium freezing temperature undergo freezing in four steps [17–19]: (1) ice-embryo nucleation, (2) recalescence, (3) solidification/freezing, and (4) cooling of the frozen droplet. Figure 1 shows a schematic representation of the droplet temperature evolution during freezing. Initially, the sessile droplet is in a liquid state below the equilibrium freezing temperature due the supercooling required for nucleation of an ice embryo. The onset of droplet freezing begins with heterogeneous nucleation

of an ice embryo at a rate that depends on surface morphology [20], the heat transferred through the contact area [8,10], the degree of supercooling of the liquid phase [21–23], droplet size, contact angle [9,24], and thermal properties of the substrate [25]. After nucleation, dendritic ice rapidly propagates throughout the droplet. The latent heat of fusion released is rapidly absorbed by the remaining fraction of the liquid droplet, which increases the temperature of the droplet to the equilibrium freezing temperature (0 °C for water) in tens of milliseconds, depending on the size of the droplet [10,17]; this process is called recalescence and labeled as (2) in Figure 1. The fraction of ice created during recalescence has been estimated by balancing the latent heat released with the sensible heat required to raise the droplet temperature to the equilibrium freezing point [17,24], which inherently assumes the process occurs adiabatically. However, certain circumstances indicate that recalescence may not occur adiabatically; for example, droplets that freeze can exhibit evaporation during recalescence, as indicated by the observation of condensed liquid droplets in a halo around the freezing droplet [26].

Immediately after recalescence, a solid ice front progresses from the droplet base to its top, freezing all the remaining liquid [17,19,27–35]. In the absence of airflow over the droplet, this solidification process results in a droplet with a symmetric conical tip [33,36], as labeled (D) in Figure 1. The rate of solidification is limited by the rate of heat dissipation to the substrate by conduction and to the environment by conduction, evaporative cooling, and convection [26,28]. As a result, the time required for complete solidification is significantly longer than the timescale of recalescence, from a fraction of a second to tens of seconds, depending on the contact angle and size of the droplet [17,24,32,37].

Models of droplet solidification have been extensively used to predict the freezing time [17,30,31,37–39]. Feuillebois and co-workers [30,31] derived analytical functions to estimate the freezing time by solving the simplified Stefan problem for droplets of fixed shapes. Chaudhary and Li [17] numerically solved the enthalpy-based heat conduction equation and considered the effect of the fraction of ice formed during recalescence. In order to capture changes in volume and variation of droplet shape during freezing, Vu et al. [38] used a front-tracking method capable of reproducing the symmetric conical tip of a frozen droplet. Zhang and coauthors [37,39] used the equivalent heat capacity method and considered the variation of thermal properties with temperature to predict the effect of contact angle [37], initial fraction of ice, and pre-recalescence temperature [39] on the freezing time. Despite these efforts, one limitation common to previous

models is that they neglect thermal coupling between the droplet and the substrate, as well as coupled heat loss and mass transfer to the environment across the droplet-air interface. Therefore, single-droplet freezing models available in the literature are not suitable for predicting the temperature and vapor concentration fields in the surrounding air, which is essential to understanding condensation halos observed in experiments [19,26] as well as the interactions between a freezing droplet and its supercooled liquid neighbors during condensation frosting [24,28].

Past experimental characterizations of heat conduction in droplets during freezing have had compromised measurement fidelity, limiting the ability to directly compare against high-fidelity numerical simulations. Intrusive and non-intrusive temperature measurement techniques have been employed to characterize single droplet freezing with either limited accuracy or spatiotemporal resolution. Chaudhary and Li [17] inserted thermocouples along the vertical centerline of a freezing droplet, which indicated that the temperature above the freezing front remains at 0 °C during most of the solidification process while the solid cools down to the temperature of the substrate, per the schematic illustration in Figure 1. However, inserting probes for temperature measurement has several drawbacks including the creation of nucleation sites, disruption of the droplet shape, and limited spatial resolution. Non-intrusive temperature measurements with better spatial resolution have been attempted with limited accuracy. Using molecular tagging thermometry, Hu and Jin [40] reported that the temperature of the liquid-ice mixture above the freezing front increased during the solidification process for a droplet consisting of a 1-BrNp·M $\beta$ -CD·ROH-water mixture, which would be unphysical for pure water. This increase in temperature was attributed to an increase in the concentration of the phosphorescence tracer molecules in the water-ice mixture that were expelled from the newly formed ice front.

Top-down view infrared (IR) thermography measurements have been used to characterize onset of droplet freezing. Li and Liu [41] recorded top-down view temperature maps during droplet freezing using IR thermography to determine the onset of freezing in pure water droplets versus droplets containing anti-freezing substances. Alizadeh et al. [10] used IR thermography to record top-down view temperature maps of the surfaces of freezing droplets to investigate the role of hydrophobicity in delaying the onset of nucleation of ice embryos. Chaudhary and Li [17] benchmarked a model for droplet solidification using temperature measurements at the top-most point of a freezing droplet using IR thermography. Top-down view infrared (IR) thermography of

droplet freezing is limited to detecting changes in high versus low temperature. Side-view IR thermography measurements of the temperature gradients in a freezing droplet due to heat conduction to the substrate have also been attempted with limited accuracy and spatial resolution. Wang and collaborators [42] reported droplet temperatures measured to unphysically increase above 0 °C after recalescence, possibly as a result of spurious reflection of thermal radiation from the surrounding environment. More recently, Graeber et al. [43] measured the temporal evolution of the spatially-averaged temperature of the surface of a freezing droplet viewed from the side; the results were used to demonstrate a rapid decline in droplet temperature, and to estimate the heat released, during sublimation caused by droplet self-dislodging.

To date, the temperature distribution during droplet freezing has not been accurately probed, which has restricted model validation to indirect comparisons with the freezing front evolution. An accurate experimental characterization of the temperature distribution, and thereby heat transfer processes occurring during droplet freezing, can lead to a better understanding of thermal coupling of the droplet with the substrate below and air in the surroundings. This paper investigates the pathways for dissipation of the latent heat released during single droplet freezing on a cooled substrate. Specifically, side-view IR thermography measurements are employed to calculate the fraction of heat dissipated to the substrate relative to the ambient air surrounding the droplet. High-spatial-resolution temperature measurements are performed inside a cold enclosure to control and reduce spurious thermal radiation from the ambient. Numerical simulations of the solidification process during droplet freezing, which account for the thermal coupling between the droplet and its environment via conduction, evaporative cooling, and natural convection, are benchmarked against experiments. The simulation results are used to quantify the fraction of latent heat released to the substrate and the surrounding air the droplet, as well as to understand the role that each transport mechanism has in altering the water vapor, temperature, and velocity fields in the air surrounding the droplet.

## **2.0. Experimental description**

An experimental facility is built to capture infrared thermography video recordings from a side view during droplet freezing. The test section (schematic diagram shown in Figure 2) is capable of cooling the substrate below freezing cooling while maintaining uniform background radiation. To minimize the influence of the background radiation and reduce spurious reflections from the



environment, the test section is surrounded by a black-painted (ColorMaster™ Flat Black, Krylon; emissivity of 0.97) aluminum enclosure that is maintained at a constant below-ambient temperature using two temperature-controlled thermoelectric stages (CP-031, TE Technology, Inc.). The sample substrates are mounted to a stackup comprising an aluminum block (sample holder in Figure 2), a thermoelectric plate (ZT8, Laird Technologies), and another aluminum block attached to the outer thermoelectric stage located at the bottom of the facility.

Smooth silicon substrate samples were cleaned and then silanized following the procedure described in Ref [44]. The sample surface had a measured average roughness of 0.001  $\mu\text{m}$  (NewView 6000, Zygo) and a contact angle of 91.5 deg using a 5  $\mu\text{l}$  water droplet (ramé-hart, 290-F1). The temperature of the sample is measured with a two-wire Pt RTD (PRTF-10-2-100-1/4-12-E-GG, Omega) placed in a hole located 2.5 mm from the top surface of the aluminum sample holder. The substrate is attached to the sample holder with carbon conductive double-sided tape (PELCO Image Tabs). The cooling system is capable of maintaining a constant set-point temperature to within  $\pm 1.0$   $^{\circ}\text{C}$  and with a measurement uncertainty of  $\pm 0.1$   $^{\circ}\text{C}$  as sensed by the RTD. This temperature signal closes a control loop that modulates the cooling power delivered by the thermoelectric plate using a temperature controller (MTTC-1410, Laird Technologies). The entire facility is mounted on micrometer stages to allow easy focusing during the IR imaging.

After a liquid water droplet is gently deposited on the substrate, the top lid of the enclosure is bolted to the lower base. Subsequently, the two cooling stages are turned on and after  $\sim 15$  min the entire test section cools down to  $-1.5$   $^{\circ}\text{C}$ . Then, the thermoelectric controller is turned on with a set-point of  $-9.0$   $^{\circ}\text{C}$ . After  $\sim 4$  min, the temperature measured by the RTD reaches a constant value within  $\pm 2\%$  of the set-point. The substrate gradually cools down to the setpoint temperature and after  $\sim 10$  min ice nucleation occurs within the droplet.

The transient temperature of the surface of the droplet is recorded at 50 fps using an infrared camera (SC7650, FLIR). A 50 mm lens (Nyctea, Janos) is connected to the camera with 38 mm extensions that provide a spatial resolution of  $0.038 \pm 0.004$  mm/pixel, where the uncertainty is taken as the standard deviation over 8 calibration measurements. A custom-made black body radiator was used to calibrate the infrared camera over a range of set-point temperatures from  $-8.5$   $^{\circ}\text{C}$  to  $22.5$   $^{\circ}\text{C}$  in  $1.0$   $^{\circ}\text{C}$  increments. At each setpoint temperature, the IR camera is used to record the digital level averaged over 100 frames. The digital level is fitted as a function of the setpoint temperature with a fourth-order polynomial for each sensor pixel. This pixel-by-pixel calibration

is applied to the experimental data. The temperature distribution on the surface of the droplets after completion of recalescence is used to correct for systemic errors caused by background radiation and nonuniform emissivity. The IR thermography data is cropped around the droplets to remove the immaterial background data. Further details on the calibration procedure applied to the IR thermography measurements are provided in the supplementary materials. IR thermography recordings on the surface of 10.1  $\mu\text{L}$  and 19.8  $\mu\text{L}$  water droplets during droplet recalescence and subsequent solidification are presented in this paper.

### **3.0. Numerical Model Description**

Numerical simulations of the transient solidification of a droplet resting on a cooled substrate are implemented in ANSYS Fluent [45]. A 2D axisymmetric model with a fixed grid is used to simulate thermal conduction in the solid substrate, solidification at the freezing front within the droplet, heat transfer and fluid flow in the droplet domain, heat and mass transfer in the surrounding gas domain, phase change, and coupled heat and mass transfer at the droplet interface. Computational domains with droplet geometry and boundary conditions matching the two freezing experiments described in Section 2.0 were implemented. The mesh and geometry (to scale) of the computational domain used for the simulation of the solidification of the 10.1  $\mu\text{L}$  droplet, indicating the key phases, interfaces, and boundaries, used in the numerical simulations is illustrated in Figure 3. All the material properties used in the numerical are summarized in Table 1. To reduce the level of complexity without sacrificing fidelity, the numerical simulations neglect the volume change due to water expansion during freezing, and therefore the volume and shape of the droplet are assumed equal to that of the droplet prior to recalescence. A maximum increase in droplet volume of  $\sim 9\%$  as a result of complete solidification would lead to a  $\sim 3\%$  increase in the height of the droplet and have negligible effect on the thermal resistance to heat flow through the frozen portion of the droplet. The following sections provide detailed descriptions of the governing equations and boundary conditions implemented in the numerical simulations.

#### **3.1. Droplet domain**

Solidification within the droplet domain is modeled using the enthalpy-porosity formulation [46,47] implemented using the solidification/melting model of ANSYS Fluent [45]. In this formulation, each computational cell is modeled with properties that are determined by a linear

relationship between the cell temperature ( $T$ ) and the fraction of liquid in the cell ( $\beta$ ). The latter is defined as:

$$\beta = \begin{cases} 0 & T < T_{sol} \\ \frac{T - T_{sol}}{T_{liq} - T_{sol}} & T_{sol} < T < T_{liq} \\ 1 & T > T_{liq} \end{cases} \quad (1)$$

where  $T_{sol}$  and  $T_{liq}$  are the liquidus and solidus temperatures for water, and  $\beta$  decreases from 1 to 0 as the material solidifies (i.e., zero liquid fraction). The narrow region between the solid and liquid phases where  $\beta$  decreases from 1 to 0 is commonly referred to as the mushy zone. Therefore, any thermophysical property  $\xi$  (i.e. specific heat or thermal conductivity) within the liquid, mushy, and solid regions can be expressed in terms of the liquid fraction as:

$$\xi = \begin{cases} \xi_s & T < T_{sol} \\ (1 - \beta)\xi_s + \beta\xi_l & T_{sol} < T < T_{liq} \\ \xi_l & T > T_{liq} \end{cases} \quad (2)$$

Considering the small length scale of the droplet and that the maximum velocity of the liquid is limited by the rate of propagation of the freezing front, laminar flow is assumed for the fluid in the liquid and porous-medium-like solid/liquid mushy zone. Under those assumptions, fluid flow within the droplet domain is modeled using the continuity and momentum equations which are expressed as:

$$\rho_l \nabla \cdot \vec{V}_l = S_{m,l} \quad (3)$$

$$\rho_l \vec{V}_l \cdot \nabla \vec{V}_l = -\nabla p_l + \mu_l \nabla^2 \vec{V}_l + S_p \quad (4)$$

where  $\mu_l$  is the viscosity of water ( $\mu_l = 1.003 \times 10^{-3}$  kg/m s),  $\vec{V}_l$  is the fluid velocity,  $S_{m,l}$  is a source term that pertains to mass transport across the interface, which is later discussed in Section 3.3, and  $S_p$  is the momentum sink due to the reduced porosity in the mushy zone. By further assuming that the flow within the mushy region is governed by Darcy's law,  $S_p$  is defined as:

$$S_p = \frac{(1-\beta)^2}{\beta^3 + \varepsilon} E_{mushy} \vec{V}_l \quad (5)$$

where  $\varepsilon$  is set equal to 0.001 to prevent division by zero when  $\beta \rightarrow 0$ , and  $E_{mushy}$  is a constant that depends on the morphology of the porous media. The value of this constant determines how fast the velocity of the material tends to zero as it solidifies, and it is set equal to  $1 \times 10^5$  in these simulations.

At each cell, the total enthalpy  $H$  is computed as the sum of the sensible enthalpy  $h$  and latent heat  $\Delta H = \beta L$  of the fraction of liquid in the cell, where  $L$  is the latent heat of solidification ( $L = 335000$  J/kg for water). Therefore, the latent heat can vary between 0 for a solid cell and  $L$  for a liquid cell. Using this definition for the total latent heat, the energy transport within the droplet domain is modeled using the energy equation which is expressed as:

$$\frac{\partial}{\partial t}(\rho h) + \nabla \cdot (\rho \vec{V} h) = \nabla \cdot (\alpha \nabla h) + S_h + S_{h,l} \quad (6)$$

where the energy source term  $S_h$  in this equation is derived from the enthalpy formulation of convection-diffusion phase change and is expressed as [48],

$$S_h = \frac{\partial(\rho \Delta H)}{\partial t} + \nabla \cdot (\rho \vec{V} \Delta H), \quad (7)$$

and the source term  $S_{h,l}$  is related to the energy transfer across the interface and is further described in Section 3.3.

### 3.2. Solid substrate and surrounding gas domains

Heat transport within the solid substrate domain is modeled assuming that the thermophysical properties of silicon do not vary within the range of temperatures considered. Under this assumption, the energy equation can be expressed as:

$$\frac{\partial T}{\partial t} = \alpha_s \nabla^2 T \quad (8)$$

To calculate fluid flow velocity, temperature, and water vapor concentration in the gas domain, it is assumed that fluid flow is laminar and Newtonian. The continuity, momentum, and energy equations are respectively:

$$\nabla \cdot (\rho_g \vec{V}_g) = S_{m,g} \quad (9)$$

$$\rho_g \vec{V}_g \cdot \nabla \vec{V}_g = -\nabla p_g + \mu_g \nabla^2 \vec{V}_g + \rho_g \vec{g} \quad (10)$$

$$\rho_g c_{p,g} \vec{V}_g \cdot \nabla T = k \nabla^2 T + S_{h,g} \quad (11)$$

where  $S_{m,g}$  and  $S_{h,g}$  are mass and energy terms later described in Section 3.3 and  $\mu_g$  is the viscosity of air ( $\mu_g = 1.789 \times 10^{-5}$  kg/m s). By further assuming that the air-vapor mixture in the gas domain follows the ideal gas law, the density of the vapor-air mixture  $\rho_g$  can be expressed as:

$$\rho_g = C_v M_{water} + \left( \frac{p_{atm}}{RT} - C_v \right) M_{air} \quad (12)$$

where  $M_{water}$  is the molecular weight of water ( $M_{water} = 0.018$  kg/mol),  $M_{air}$  is the molecular weight of dry air ( $M_{air} = 0.029$  kg/mol), and the mole concentration of water vapor in the mixture  $C_v$  is solved with the following governing equation for diffusive and convective transport in the gas domain:

$$\vec{V}_g \cdot \nabla C_v - \nabla \cdot (D \cdot \nabla C_v) = 0 \quad (13)$$

In equation (13), the temperature-dependent diffusion coefficient  $D$  is given by:

$$D(T) = D_{ref} \left( \frac{T}{T_{ref}} \right)^{1.5} \quad (14)$$

Further details on the implementation of equation (13) using user-defined scalar (UDS) functions in Fluent is provided in the supplementary materials.

### 3.3. Droplet-gas interface

Heat and mass transport across the interface between the droplet and gas domains is modeled by neglecting the effects of capillary pressure and interfacial phase-change resistances across the droplet-gas interface. The effects of a capillary pressure difference across the interface during droplet condensation and freezing are known to be negligible for droplets with radius larger than  $\sim 1 \mu\text{m}$  [49]. In the presence of non-condensable gases (i.e., for an air-water mixture), the interfacial resistances to condensation and evaporation are significantly smaller than the resistance to diffusion of vapor. Therefore, the saturation vapor pressure is calculated based on the local temperature of the droplet-gas interface. Because the saturation vapor pressure above an ice

surface is smaller than above a supercooled liquid water surface at the same temperature [50], the saturation vapor pressure also depends on the local fraction of ice on the surface of the droplet. To simplify implementation in the numerical simulations, cells on the face of the droplet-air interface above 0 °C are treated as liquid, whereas cells that are below 0 °C are treated as ice. Expressions for the saturation vapor pressure above ice and supercooled liquid surface, as well as further details on the implementation of user-defined functions to calculate the content of water inside the air domain are provided in the supplementary materials.

At the liquid-gas interface, shear stress along both sides of the interface are set as zero and the vapor flux across the interface, which can be induced by condensation or evaporation depending on the local vapor saturation pressure at the surface, is expressed as:

$$m'' = M_v \left( -D\vec{n} \cdot \nabla C_v + v_n C_v \right) \quad (15)$$

where the first term inside the parentheses on the right-hand side is the vapor transport due to mass diffusion, and the second term represents mass convection by Stefan flow. Because dry air does not pass through the droplet-gas interface, the flux of air is set to zero at the interface:

$$0 = M_g \left( -D\vec{n} \cdot \nabla (C_g - C_v) + v_n (C_g - C_v) \right) \quad (16)$$

Therefore, the velocity of the vapor crossing the interface can be expressed as:

$$v_n = -\frac{1}{C_g - C_v} D(\vec{n} \cdot \nabla C_v) \quad (17)$$

By coupling equations (15) and (17), the mass flux at the interface can be written as:

$$m'' = -\frac{M_v D}{1 - C_v/C_g} (\vec{n} \cdot \nabla C_v), \quad (18)$$

where the vapor molar concentration in the gas and the vapor at the interface are respectively calculated as  $C_g = p_{atm}/RT_{lv}$  and  $C_v = p_{atm}(T_{lv})/RT_{lv}$ .

The mass transport across the interface is modeled by adding mass sources and sinks to the mesh cells adjacent to either side of the interface, following an analogous procedure as explained in Refs. [51,52]:

$$S_{m,g} = \frac{m'' A_{cell}}{V_{cell,g}} \quad (19)$$

$$S_{m,l} = -\frac{m'' A_{cell}}{V_{cell,l}} \quad (20)$$

where  $A_{cell}$  is the interface area of the specified cell adjacent to the interface and  $V_{cell}$  is the cell volume. Energy transport induced by evaporation and condensation processes are modeled by adding energy sources in the mesh cells adjacent to the interface on either side:

$$S_{h,g} = S_{m,g} h_s(T) \quad (21)$$

$$S_{h,l} = S_{m,l} h_s(T) + S_{m,l} h_{f,g} \quad (22)$$

$$h_s(T) = c_p (T - T_{ref}) \quad (23)$$

The first terms on the right-hand sides of equations (21) and (22) represent the sensible heat contributed by the mass source, while the additional term in equation (22) accounts for the latent heat adsorbed/released during evaporation/condensation, where  $h_{f,g}$  is the latent heat of evaporation ( $h_{f,g} = 2.497 \times 10^6$  J/kg). The temperature  $T_{ref}$  in equation (23) is an arbitrary reference temperature implemented in the simulation set equal to 0 °C.

### 3.4. Other boundary conditions

At the outer boundary of the gas domain, 100 times larger than the droplet radius, the concentration of vapor is calculated using:

$$C_v = \frac{RH p_{sat}(T_\infty)}{RT_\infty}, \quad (24)$$

where  $RH$  is the relative humidity of the air and  $T_\infty$  is the temperature of the air in the far field. For all the simulations presented in this paper, the relative humidity and ambient temperature were set respectively equal to 30 % and -1.5 °C.

The average of the contact line temperature measured from the experiments is used as a time-dependent boundary condition at each cell in the bottom of the droplet domain employing UDFs. The temperature at the bottom of the substrate is set constant and equal to the set-point temperature of the thermoelectric controller. To ensure thermal coupling between all the interior boundaries in the domain, the temperature across these boundary was assumed to be continuous  $T_1 = T_2$  and any contact thermal resistances are neglected  $k_1 (n_1 \cdot \nabla T_1) = k_2 (n_2 \cdot \nabla T_2)$ .

### 3.5. Initial conditions

Prior to formation of the freezing front, i.e., the solid ice that progresses from the bottom to the top of the droplet, some fraction of the liquid is frozen as dendrites during the recalescence process (as described alongside discussion of Figure 1). The fraction of this ice formed it is often calculated by equating all the latent heat it releases to the sensible heat required to increase the supercooled droplet temperature up to 0 °C via an adiabatic process. In this work, the initial fraction of ice is estimated considering energy losses to the surroundings of the droplet. Therefore, the latent heat released during recalescence is equated to the heat loss to the surroundings in addition to the sensible heating of the formed ice and the remaining liquid up to 0 °C:

$$\frac{\rho_l v x \Delta H}{\Delta t_{rec}} = \frac{\rho_l v x c_{p,s} \Delta T}{\Delta t_{rec}} + \frac{\rho_l v (1-x) c_{p,l} \Delta T}{\Delta t_{rec}} + q_{rec,loss} \quad (25)$$

where  $x = 1 - \beta$  is the fraction of ice,  $\Delta t_{rec}$  is the duration of recalescence,  $v$  is the volume of the droplet before recalescence, and  $q_{rec,loss}$  is the total heat transferred to the ambient air and to the substrate during recalescence. The heat loss,  $q_{rec,loss}$ , is estimated by numerically solving the rate of heat transfer between the droplet at 0 °C and its surroundings (i.e., the substrate and gas domains with boundary conditions described above) under quasi-steady conditions. The temperature distributions in the in the gas and solid domains obtained from these quasi-steady simulations are also used as the initial conditions in the transient simulation of solidification. The initial fraction of liquid calculated using equation (25) is used in equation (1) to calculate  $T_{sol}$  and  $T_{liq}$ , which are then input as initial conditions to the solidification/melting model to set the corresponding initial fraction of liquid. Heat losses during recalescence of the 10.1  $\mu\text{L}$  and 19.8  $\mu\text{L}$  droplets were estimated to be 25 W and 42 W, which correspond to initial fractions of ice equal to 0.17 and 0.21, respectively.

### 3.6. Numerical solution settings

After calculating the initial fraction of ice and the initial temperature fields within all the computational domains using the method described in Section 3.5, the numerical solution of the transient solidification is set to use the SIMPLE algorithm for pressure-velocity coupling and the first-order implicit scheme for time-discretization, with a time step of 0.01 s. To confirm that the results are independent of the geometrical characteristics of the computational domain such as



mesh and domain dimensions. A mesh size independence check was performed to confirm that the results are insensitive to further mesh refinement a mesh with twice as many cells resulted in less than a 1% change in the freezing time. To confirm the results are independent of the size of the domain, simulations were performed to show that the freezing time changed less than 1% when the size of the domain were increased from 20 to 100 times the droplet radius. The mesh used (shown in Figure 2), for the case of a 10.1  $\mu\text{L}$  droplet, has a total of 119,450 quadrilateral cells. Similar mesh and domain sizes were employed for the 19.8  $\mu\text{L}$  droplet case.

## 4.0. Results

This section presents the transient infrared (IR) surface temperature data acquired during the recalescence and solidification processes of individual droplets having two different volumes of 10.1  $\mu\text{L}$  and 19.8  $\mu\text{L}$ . These measurements are used to reveal details of the crystallization dynamics during recalescence in Section 4.1 and to benchmark the model for droplet solidification in Section 4.2. In Section 4.3, the temperature, water vapor concentration, and velocity fields obtained from the numerical simulations are used to qualitatively assess the different transport mechanisms that participate in the dissipation of latent heat from a solidifying droplet to its environment. A quantitative description of each pathway for latent heat dissipation is provided in Section 0.

### 4.1. *Crystallization dynamics during recalescence*

Side-view infrared surface temperature maps of the droplet during recalescence reveal details of the relationship between the crystallization dynamics and heat transfer. A sequence of snapshots showing the evolution of the temperature distribution on the surface of 10.1  $\mu\text{L}$  and 19.8  $\mu\text{L}$  droplets undergoing recalescence are shown in Figure 4. Immediately prior recalescence at  $t = 0$  s, both droplets are in the liquid state and have been supercooled to an average surface temperature of approximately  $-8.3$   $^{\circ}\text{C}$ . At this stage, there is a slight vertical temperature gradient in the liquid due to heat conduction from the droplet to the substrate, with a total temperature differential across the droplet height on the order of  $\sim 1$   $^{\circ}\text{C}$ . Subsequently at  $t = 0.02$  s, ice crystals heterogeneously nucleate at the base of the droplet in contact with the substrate and begin to propagate towards the top of the droplet. The temperature maps indicate two well-defined regions, each with a near-uniform temperature distribution, that are separated by a sharp temperature gradient which defines

the crystallization front. Regions ahead of the crystallization front remain in the supercooled liquid state at  $-8.3\text{ }^{\circ}\text{C}$  whereas the temperature of the water ice-mixture, in the region where crystallization has occurred, becomes close to the equilibrium freezing temperature of  $0.0\text{ }^{\circ}\text{C}$ . At later times, throughout propagation of the crystallization front, additional crystallization maintains the temperature of this water-ice mixture close to  $0.0\text{ }^{\circ}\text{C}$ .

The crystal growth dynamics during recalescence are known to be related to the degree of supercooling of the liquid phase [21–23], droplet size, contact angle [9,24], and thermal properties of the substrate [25]. The sequence of images shown in Figure 4 provide evidence that the crystallization front propagates at a slightly lower velocity in the droplet of a larger size. For the  $10.1\text{ }\mu\text{L}$  and  $19.8\text{ }\mu\text{L}$  droplets with heights of  $1.72\text{ mm}$  and  $2.10\text{ mm}$ , the total times to complete recalescence are  $0.10\text{ s}$  and  $0.14\text{ s}$ , respectively. This corresponds to average crystallization front velocities of  $17.2\text{ mm/s}$  and  $15.0\text{ mm/s}$ , which are in accordance with a typical crystallization speed of  $\sim 10\text{ mm/s}$  measured for films on substrates with thermal conductivities similar to silicon [25]. Further, a decelerating rate of crystal growth shown in the sequence of images in Figure 4 indicates a spatial dependence of the crystallization dynamic. In the first few hundredths of seconds during recalescence, between  $0.00\text{ s} < t < 0.06\text{ s}$ , the crystallization front proceeds much faster ( $\sim 34\text{ mm/s}$ ) than at later times  $t > 0.06\text{ s}$ , when the crystallization front advances at  $\sim 8\text{ mm/s}$ . As the front progresses, and the mass of liquid water in the water-ice mixture available to absorb the latent heat released reduces, this reduces the rate at which crystallization occurs. Similar results have been reported by Jung *et al.* [9] while tracking the evolution of the crystallization front using high-speed side-view optical visualization.

#### **4.2. Temperature distribution on the surface of solidifying droplets**

The droplet surface temperature maps measured from IR thermography during droplet solidification (after recalescence) are used to benchmark the numerical simulations by direct comparison. Figure 5 presents a sequence of side-view surface temperature contours at several time steps during the solidification of  $10.1\text{ }\mu\text{L}$  and  $19.8\text{ }\mu\text{L}$  droplets. The temperature plots obtained from the simulations are shown for a full droplet by revolving the droplet-gas interface temperature around the axis of symmetry of the computational domain. Overall, the numerical simulation qualitatively matches the measured temperature distribution and time to complete solidification, with further discussion below.

The sequence of side-view surface temperature contours presented in Figure 5 shows that, at each time interval between droplet recalescence and complete solidification, the portion of the droplet above the solidification front remains at a temperature close to the freezing equilibrium temperature of  $0.0\text{ }^{\circ}\text{C}$ , with any variations on the order of the temperature resolution. Meanwhile, a well-defined temperature gradient develops within the growing ice layer below the solidification front. As the solidification front pushes the water-ice mixture upward, the tip of the droplet forms a conical apex in the experiments, which is not present in the simulation results because volume changes during the solidification process are neglected. These results confirm that this does not lead to significant deviations in the temperature or freezing times when compared with the experiments. Once solidification has occurred throughout the droplet volume, the frozen droplet cools down to a temperature near the temperature of the substrate ( $-9.0\text{ }^{\circ}\text{C}$ ).

A more quantitative comparison between the IR thermography and simulation data is presented in the plots of the temperature along the interface shown in Figure 6, where the length along the arc ( $s$ ) is normalized by the radius ( $R$ ) such that  $s/R = 0$  represents the contact line of the droplet and  $s/R = 1$  corresponds the tip of the droplet. For example, at  $t = 5.10\text{ s}$  in Figure 6 (a), the temperature of the droplet at the contact line of the droplet ( $s/R = 0$ ) is  $-4.82\text{ }^{\circ}\text{C}$  and increases with  $s/R$  up to  $T_{eq}$ , which corresponds to the location of the solidification front at  $s/R = 0.27$ . Along the section of the interface that has not yet solidified,  $0.27 < s/R < 1.0$  the temperature remains close to  $T_{eq}$ . At subsequent times, as the solidification front advances towards the tip of the droplet, the temperature at the contact line of the droplet decreases. When the solidification process completes at  $t = 21.70\text{ s}$ , the temperature difference between the contact line and tip of the droplet is due to conduction through the solid droplet. At each location on the surface of the droplet, throughout the solidification process for both the  $10.1\text{ }\mu\text{L}$  and  $19.8\text{ }\mu\text{L}$  droplets, the average relative error between the measured and simulated temperatures is below 4.1%, indicating that the numerical simulation approach accurately captures the governing mechanisms that drive heat transfer during droplet solidification.

Overall, the surface temperature plots along the normalized arc length during solidification of the  $19.8\text{ }\mu\text{L}$  droplet present similar trends as for the  $10.1\text{ }\mu\text{L}$  droplet, except for one subtle difference worth noting. At any given time after recalescence, for example after approximately 5 s, 10 s and 15 s, the temperature at the contact line of the  $10.1\text{ }\mu\text{L}$  droplet is slightly lower when compared to the temperature at the contact line of the  $19.8\text{ }\mu\text{L}$  droplet. This is because the  $10.1$

$\mu\text{L}$  droplet is at a later stage of the solidification process for which a larger percentage of the water has solidified. This strong dependence of the substrate temperature with time clearly indicates that a time-dependent boundary condition at the base of the droplets must be considered.

#### **4.3. Mechanisms of heat and mass exchange between the droplet and surroundings**

In this section, the temperature and liquid fraction distributions within the  $10.1 \mu\text{L}$  droplet, as well as the water vapor mass fraction and the velocity vector field in the gas domain (near the gas-droplet interface), are used to identify the mechanisms that drive heat and mass transport from a freezing droplet to its environment. A time sequence of the temperature distribution contours in the simulation domain near the droplet are shown in Figure 7 (a). The temperature gradients in the contours suggest two primary paths of heat transfer: (1) from the droplet to the solid substrate and (2) from the droplet to the surrounding ambient gas. Different mechanisms drive heat transfer through each of these pathways. Within the solid substrate domain, heat conduction is driven by the temperature difference between the base contact area of the droplet and the lower wall of the substrate. Whereas in the gas domain, the temperature and concentration differences between the droplet-gas interface and its surroundings drives combined diffusion and convection, as well as phase change at the droplet-air interface, with characteristics that depend on the stage of the solidification process. The influence of each one of these transport mechanisms on the solidification process is assessed in Sections 4.3.1, 4.3.2, and 4.3.3.

##### **4.3.1. Heat diffusion in the solid substrate**

Just after the recalescence process, at  $t = 0.10 \text{ s}$  in Figure 7 (a), the temperature distribution within the substrate shows that a portion of the heat released during recalescence locally heats the substrate below the droplet and the air near the droplet-gas interface. The temperature difference between the droplet-substrate interface and the lower wall of the substrate drives heat away from the droplet and spreads laterally within the substrate and into the ambient air. As the solidification process advances (e.g.,  $t = 10.10 \text{ s}$ ), the latent heat released at the solidification front is conducted through the solidified part of the droplet to the substrate and the air around the droplet. This results in a temperature field inside the droplet with isotherms that increase in the direction from the the location of the freezing front to the base. The thermal resistance of the solid part of the droplet increases as the solidification front advances, which causes a decrease in the temperature at droplet-substrate interface. As a result, heat diffusion within the substrate reduces as solidification

proceeds. At  $t = 21.70$  s, when the droplet has completely solidified, the temperature difference between the droplet base and the lower wall of the substrate reduces significantly.

#### **4.3.2. Heat transport in the gas domain**

The temperature difference between the droplet-gas interface and its surroundings (both the far-field air temperature and the substrate temperature) not only drives heat diffusion away from the droplet through the air domain, but it also creates density gradients that drive flow in the air domain. Figure 7 (b) shows a time sequence of velocity vector fields in the gas domain along with the liquid fraction in the droplet during the solidification of the  $10.1 \mu\text{L}$  droplet. At the onset of the solidification ( $t = 0.10$  s in Figure 7 (b)), cold air flows from regions of the gas domain located on the sides of the droplet toward hotter regions of the gas domain above the droplet. At subsequent times, when the solidification front has progressed within the droplet, heat exchange via diffusion and convection are localized to within the section of the interface above the solidification front, which remains close to  $0^\circ\text{C}$ . At  $t = 10.10$  s in Figure 7 (b), the additional cooling produced by the combined effect of the heat diffusion, natural convection, and evaporation drives additional solidification within the region of the droplet near the droplet-gas interface. Meanwhile, due to a decreasing interface temperature in the region behind the solidification front, the mean velocity of air flow decreases, which reduces the cooling induced by natural convection. Once the solidification process is completed, water vapor is driven away from the droplet due to a small concentration difference from the surface of the droplet to the far field.

#### **4.3.3. Mass transport in the gas domain and evaporative cooling at the gas-droplet interface**

A time sequence of mass vapor fraction contour plots in the gas domain around the  $10.1 \mu\text{L}$  droplet is shown in Figure 7 (c). The concentration gradients indicate that evaporated water vapor is transported away from the droplet-gas interface to the ambient via both vapor diffusion and convection. At the onset of the formation of the solidification front ( $t = 0.10$  s), the mass fraction of water vapor in the air near the droplet-gas interface is uniform and about four times larger than the fraction of water vapor far away from the interface. This water vapor gradient drives diffusion of water vapor into the ambient air. However, in contrast to the hemispherically uniform water vapor fraction field produced by an evaporating droplet driven by vapor diffusion alone, convection alters the iso-concentration contours (as shown at  $t = 0.10$  s in Figure 7 (c)). Dry air flowing in

from the sides of the droplet induces stronger evaporation near the contact line of the droplet than near the top of droplet. Differences in temperature along the interface induced by evaporative cooling are not appreciable in the temperature contours because they are suppressed by the additional solidification process occurring within the droplet after recalescence. At  $t = 10.10$  s, the concentration of water reduced in the air near the droplet surface below the solidification front, which localizes evaporation to the region above the solidification front. When the droplet has solidified, the saturation pressure above the surface of the frozen droplet is smaller than the concentration of vapor far away from the droplet, driving vapor diffusion away from the droplet-gas interface. This prediction of the complete temperature and vapor concentration field around the droplet can be used for understanding the interaction of a freezing droplet with its environment. For example, these temperature and concentration fields along the substrate near the droplets could be used as a tool to study the formation of condensation halos with higher fidelity than previous literature.

#### ***4.4. Pathways for heat dissipation during droplet solidification***

The solidification modeling results are used to calculate the fraction of latent heat that is transferred to the substrate versus the ambient air. The total heat transfer rate through the substrate contact area, as well as separately integrated over the droplet-gas interface, at each time step during the solidification process is shown in Figure 8 (a) for the 10.1  $\mu\text{L}$  and 19.8  $\mu\text{L}$  droplets. The heat transfer through the droplet-gas interface is separately delineated in Figure 8 (b) between the mechanism of evaporative cooling and the combined contributions of heat diffusion and natural convection cooling. At early stages of the solidification process, the latent heat released rapidly increases to its maximum value; as the solidification front progresses, the heat transfer rates through the substrate and the droplet interface decrease. As it was described in Sections 4.2 and 4.3, heat diffusion transfer to the solid substrate is limited by the thermal resistance of the solid part of the droplet behind of the solidification front, which increases as the solidification front advances. Meanwhile, heat transfer across the droplet interface reduces due to the combined effect of: (1) heat and mass diffusion becomes confined to the upper section of the droplet surface ahead of the solidification front; and (2) a reduction of the convective heat and mass transport that results from a decrease in the velocity of the dry air drawn in from the sides of the droplet. In general, the heat transferred through the interfaces of the droplet depends on the area, and therefore the heat transfer rates are lower for the 10.1  $\mu\text{L}$  compared to the 19.8  $\mu\text{L}$  droplet.

Throughout the entire duration of the solidification process, the fraction of latent heat that is transferred to the substrate is at least one order of magnitude larger than the heat transferred to the ambient air. For the 10.1  $\mu\text{L}$  droplet, the maximum heat transfer rate crossing the droplet-gas interface is  $5.9 \times 10^{-3}$  W, while the maximum heat transfer rate across the contact area is about 68 times larger at  $4.0 \times 10^{-1}$  W (the ratios are similar for the 19.8  $\mu\text{L}$  droplet). Therefore, conditions that alter the diffusion of heat to the substrate (e.g., substrate thermal conductivity, droplet contact angle) would have a more severe impact on the dynamics of solidification than changes in ambient conditions (e.g., ambient temperature and relative humidity). However, considering the effects of the ambient conditions is nevertheless essential for a complete description of the interactions of a freezing droplet with its environment. Because droplet freezing rarely occurs in isolation, prediction of the interaction between a droplet and its environment presented in this paper provide a framework for understanding the propagation of frost, which depends on the evaporation of supercooled liquid neighbors and ice bridging with other liquid droplets.

## 5.0. Conclusions

This work uses infrared (IR) temperature measurements on the surface of a freezing droplet, as well as a numerical simulation benchmarked with a direct comparison of the temperature maps, to quantitatively describe the transport mechanisms that determine the pathways for latent heat dissipation from a droplet freezing on a cooled substrate to its surroundings. The experimental technique used in this work demonstrates that, by reducing ambient radiation during sub-freezing infrared (IR) measurements, temperature maps with high spatial resolution can be used to track the evolution of the crystallization front during droplet recalescence, as well as to resolve the temperature gradients at the surface of solidifying microliter droplets. Contrary to highly simplified models for the describing the interaction between a freezing droplet and its surroundings that are available in the literature (e.g., adiabatic recalescence, constant droplet base temperature, adiabatic droplet-gas interface), the modeling approach presented in this paper uses the IR temperature data at the contact line of the droplet as boundary condition and provides a full description of the driving mechanisms for heat and mass exchange between a freezing droplet, the substrate, and the ambient air. These combined advances enable the experimental and modeling approach presented in this paper to not only track the dynamic of the solidification front, but to directly compare the temperature maps (with average error below 4.1%).

The simulation results indicate that heat transfer rate to the substrate of the droplet is at least one order of magnitude greater than the heat transferred to the ambient air. Most of the latent heat released during the solidification process spreads within the substrate, whereas the small portion of the latent heat that is lost to the ambient air is concentrated in the region of the droplet surface above the solidification front. Heat exchange via heat conduction, natural convection, and evaporative cooling at the droplet-gas interface lead to corresponding changes in the ambient temperature, velocity, and vapor concentration fields around the droplet. Evaporative cooling only accounted for a small percentage of the total heat exchange at the droplet-gas interface, whereas the combined heat diffusion and natural convection accounted for most of the cooling at the droplet-gas interface.

In spite of the seemingly small role of the heat and mass transport through the droplet-gas interface in the solidification of a single droplet, in terms of the total heat exchange, it nevertheless has a critical influence on the mechanisms that govern frost propagation. Droplet freezing rarely occurs in isolation, but rather, during condensation freezing, individual droplets freeze while exchanging heat and mass with neighboring supercooled and frozen droplets. The methodology presented in this paper, which accurately describes the heat and mass transfer process between a freezing droplet and its environment, may be a powerful tool for understanding the interactions between a freezing droplet and its neighbors during the propagation of frost on a cooled substrate, as well as the evaporation of neighboring droplets during condensation halo formation.

## **Acknowledgments**

The first author acknowledges financial support provided by the Colombian Department for Science, Technology and Innovation (Colciencias), Fulbright-Colombia and the Colombia-Purdue Institute (CPI).

## **References**

- [1] R.W. Gent, N.P. Dart, J.T. Cansdale, Aircraft icing, *Philosophical Transactions: Mathematical, Physical and Engineering Sciences*. 358 (2000) 2873–2911.
- [2] Y. Cao, Z. Wu, Y. Su, Z. Xu, Aircraft flight characteristics in icing conditions, *Progress in Aerospace Sciences*. 74 (2015) 62–80.
- [3] D.-Y. Lee, M.-Y. Lee, Y. Kim, Experimental study on frost height of round plate fin-tube heat exchangers for mobile heat pumps, *Energies*. 5 (2012) 3479–3491.



- [4] O. Parent, A. Ilinca, Anti-icing and de-icing techniques for wind turbines: Critical review, *Cold Regions Science and Technology*. 65 (2011) 88–96.
- [5] J.L. Laforte, M.A. Allaire, J. Laflamme, State-of-the-art on power line de-icing, *Atmospheric Research*. 46 (1998) 143–158.
- [6] M. Amer, C.-C. Wang, Review of defrosting methods, *Renewable and Sustainable Energy Reviews*. 73 (2017) 53–74
- [7] L. Fay, X. Shi, Environmental impacts of chemicals for snow and ice control: state of the knowledge, *Water Air Soil Pollution*. 223 (2012) 2751–2770
- [8] P. Tourkine, M. Le Merrer, D. Quéré, Delayed freezing on water repellent materials, *Langmuir*. 25 (2009) 7214–7216.
- [9] S. Jung, M. Dorrestijn, D. Raps, A. Das, C.M. Megaridis, D. Poulidakos, Are superhydrophobic surfaces best for icephobicity?, *Langmuir*. 27 (2011) 3059–3066.
- [10] A. Alizadeh, M. Yamada, R. Li, W. Shang, S. Otta, S. Zhong, L. Ge, A. Dhinojwala, K.R. Conway, V. Bahadur, A.J. Vinciguerra, B. Stephens, M.L. Blohm, Dynamics of ice nucleation on water repellent surfaces, *Langmuir*. 28 (2012) 3180–3186.
- [11] J.B. Boreyko, R.R. Hansen, K.R. Murphy, S. Nath, S.T. Retterer, C.P. Collier, Controlling condensation and frost growth with chemical micropatterns, *Scientific Reports*. 6 (2016) 19131.
- [12] X. Sun, Bioinspired anti-icing coatings and spatial control of nucleation using engineered integral humidity sink effect, Ph.D., Arizona State University, 2017.
- [13] T.M. Schutzius, S. Jung, T. Maitra, P. Eberle, C. Antonini, C. Stamatopoulos, D. Poulidakos, Physics of icing and rational design of surfaces with extraordinary icephobicity, *Langmuir*. 31 (2015) 4807–4821.
- [14] P. Eberle, M.K. Tiwari, T. Maitra, D. Poulidakos, Rational nanostructuring of surfaces for extraordinary icephobicity, *Nanoscale*. 6 (2014) 4874–4881.
- [15] F. Wang, Y. Zhou, W. Yang, M. Ni, X. Zhang, C. Liang, Anti-frosting performance of sprayable superhydrophobic coating suitable for outdoor coil of air source heat pump, *Applied Thermal Engineering*. 169 (2020) 114967.
- [16] K.S. Boyina, A.J. Mahvi, S. Chavan, D. Park, K. Kumar, M. Lira, Y. Yu, A.A. Gunay, X. Wang, N. Miljkovic, Condensation frosting on meter-scale superhydrophobic and superhydrophilic heat exchangers, *International Journal of Heat and Mass Transfer*. 145 (2019) 118694.
- [17] G. Chaudhary, R. Li, Freezing of water droplets on solid surfaces: An experimental and numerical study, *Experimental Thermal and Fluid Science*. 57 (2014) 86–93.
- [18] X. Zhang, X. Wu, J. Min, Freezing and melting of a sessile water droplet on a horizontal cold plate, *Experimental Thermal and Fluid Science*. 88 (2017) 1–7.
- [19] S. Jung, M.K. Tiwari, N.V. Doan, D. Poulidakos, Mechanism of supercooled droplet freezing on surfaces, *Nature Communications*. 3 (2012) 615.
- [20] L. Cao, A.K. Jones, V.K. Sikka, J. Wu, D. Gao, Anti-icing superhydrophobic coatings, *Langmuir*. 25 (2009) 12444–12448.
- [21] S.H. Tirmizi, W.N. Gill, Effect of natural convection on growth velocity and morphology of dendritic ice crystals, *Journal of Crystal Growth*. 85 (1987) 488–502.
- [22] J.S. Langer, R.F. Sekerka, T. Fujioka, Evidence for a universal law of dendritic growth rates, *Journal of Crystal Growth*. 44 (1978) 414–418.

- [23] W.J. Boettinger, J.A. Warren, The phase-field method: simulation of alloy dendritic solidification during recalescence, *Metallurgical and Materials Transactions A*. 27 (1996) 657–669.
- [24] S. Chavan, D. Park, N. Singla, P. Sokalski, K. Boyina, N. Miljkovic, effect of latent heat released by freezing droplets during frost wave propagation, *Langmuir*. 34 (2018) 6636–6644.
- [25] W. Kong, H. Liu, A theory on the icing evolution of supercooled water near solid substrate, *International Journal of Heat and Mass Transfer*. 91 (2015) 1217–1236.
- [26] S. Jung, M.K. Tiwari, D. Poulikakos, Frost halos from supercooled water droplets, *Proceedings of the National Academy of Sciences*. 109 (2012) 16073–16078.
- [27] J. Guadarrama-Cetina, A. Mongruel, W. González-Viñas, D. Beysens, Percolation-induced frost formation, *Europhysics Letters*. 101 (2013) 16009.
- [28] S. Nath, S.F. Ahmadi, J.B. Boreyko, A review of condensation frosting, *Nanoscale and Microscale Thermophysical Engineering*. 21 (2017) 81–101.
- [29] L. Yin, Q. Xia, J. Xue, S. Yang, Q. Wang, Q. Chen, In situ investigation of ice formation on surfaces with representative wettability, *Applied Surface Science*. 256 (2010) 6764–6769.
- [30] F. Feuillebois, A. Lasek, P. Creismas, F. Pigeonneau, A. Szaniawski, Freezing of a subcooled liquid droplet, *Journal of Colloid and Interface Science*. 169 (1995) 90–102.
- [31] S. Tabakova, F. Feuillebois, On the solidification of a supercooled liquid droplet lying on a surface, *Journal of Colloid and Interface Science*. 272 (2004) 225–234.
- [32] L. Huang, Z. Liu, Y. Liu, Y. Gou, L. Wang, Effect of contact angle on water droplet freezing process on a cold flat surface, *Experimental Thermal and Fluid Science*. 40 (2012) 74–80.
- [33] Z. Jin, S. Jin, Z. Yang, Visualization of icing process of a water droplet impinging onto a frozen cold plate under free and forced convection, *J Vis*. 16 (2013) 13–17.
- [34] L. Karlsson, A numerical and experimental investigation of the internal flow of a freezing water droplet, *Digitala Vetenskapliga Arkivet*, (2015).
- [35] T.V. Vu, G. Tryggvason, S. Homma, J.C. Wells, Numerical investigations of drop solidification on a cold plate in the presence of volume change, *International Journal of Multiphase Flow*. 76 (2015) 73–85.
- [36] J.H. Snoeijer, P. Brunet, Pointy ice-drops: How water freezes into a singular shape, *American Journal of Physics*. 80 (2012) 764–771.
- [37] H. Zhang, Y. Zhao, R. Lv, C. Yang, Freezing of sessile water droplet for various contact angles, *International Journal of Thermal Sciences*. 101 (2016) 59–67.
- [38] T.V. Vu, K.V. Dao, B.D. Pham, Numerical simulation of the freezing process of a water drop attached to a cold plate, *Journal of Mechanical Science and Technology*. 32 (2018) 2119–2126.
- [39] X. Zhang, X. Liu, X. Wu, J. Min, Simulation and experiment on supercooled sessile water droplet freezing with special attention to supercooling and volume expansion effects, *International Journal of Heat and Mass Transfer*. 127 (2018) 975–985.
- [40] H. Hu, Z. Jin, An icing physics study by using lifetime-based molecular tagging thermometry technique, *International Journal of Multiphase Flow*. 36 (2010) 672–681.
- [41] F.F. Li, J. Liu, Thermal infrared mapping of the freezing phase change activity of micro liquid droplet, *Journal of Thermal Analysis and Calorimetry*. 102 (2010) 155–162.
- [42] Y. Wang, Z. Wang, Sessile droplet freezing on polished and micro-micro-hierarchical silicon surfaces, *Applied Thermal Engineering*. 137 (2018) 66–73.

- [43] G. Graeber, V. Dolder, T.M. Schutzius, D. Poulikakos, Cascade freezing of supercooled water droplet collectives, *ACS Nano*. (2018) 12 (2018) 11274–11281.
- [44] J.E. Castillo, J.A. Weibel, Predicting the growth of many droplets during vapor-diffusion-driven dropwise condensation experiments using the point sink superposition method, *International Journal of Heat and Mass Transfer*. 133 (2019) 641–651.
- [45] ANSYS, Inc., ANSYS FLUENT 19.4 User's Guide, (2019).
- [46] V.R. Voller, C. Prakash, A fixed grid numerical modelling methodology for convection-diffusion mushy region phase-change problems, *International Journal of Heat and Mass Transfer*. 30 (1987) 1709–1719.
- [47] V.R. Voller, C.R. Swaminathan, Eral source-based method for solidification phase change, *Numerical Heat Transfer, Part B: Fundamentals*. 19 (1991) 175–189.
- [48] V.R. Voller, M. Cross, N.C. Markatos, An enthalpy method for convection/diffusion phase change, *International Journal for Numerical Methods in Engineering*. 24 (1987) 271–284.
- [49] S. Nath, J.B. Boreyko, On localized vapor pressure gradients governing condensation and frost phenomena, *Langmuir*. 32 (2016) 8350–8365.
- [50] D.M. Murphy, T. Koop, Review of the vapour pressures of ice and supercooled water for atmospheric applications, *Quarterly Journal of the Royal Meteorological Society*. 131 (2005) 1539–1565.
- [51] H. Wang, J.Y. Murthy, S.V. Garimella, Transport from a volatile meniscus inside an open microtube, *International Journal of Heat and Mass Transfer*. 51 (2008) 3007–3017.
- [52] Z. Pan, S. Dash, J.A. Weibel, S.V. Garimella, Assessment of water droplet evaporation mechanisms on hydrophobic and superhydrophobic substrates, *Langmuir*. 29 (2013) 15831–15841.

## Figures

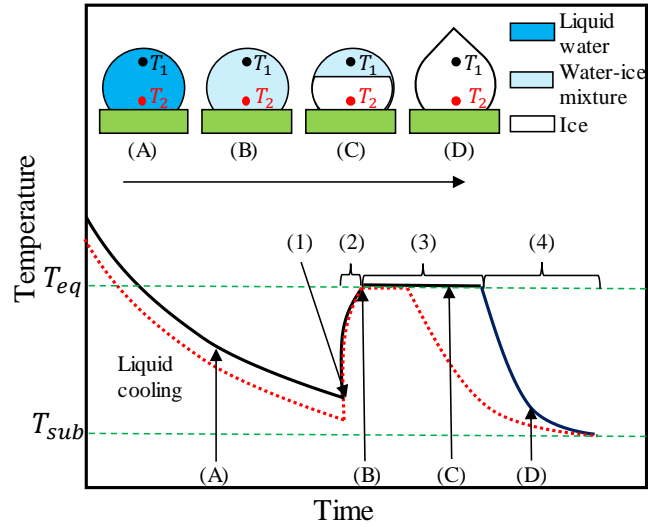


**Figure 1.** Schematic diagram of the temperature evolution during droplet freezing on a substrate that has been cooled down to  $T_{sub}$ , below equilibrium freezing temperature,  $T_{eq}$ . Two temperature traces are provided for the base ( $T_1$ , dashed red line) and the top ( $T_2$ , solid black line) of the droplet as indicated in the inset sketches. Inset droplet schematics (A)-(D) correspond to specific times within each one of the four stages of freezing (1)-(4).

Note for the editor: Single column figure

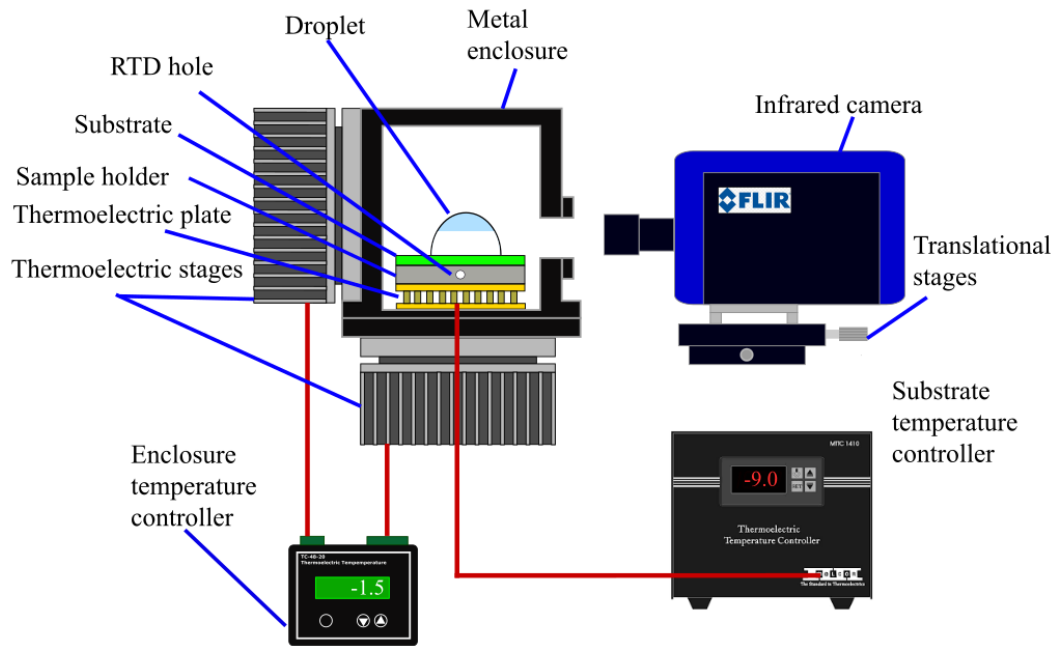
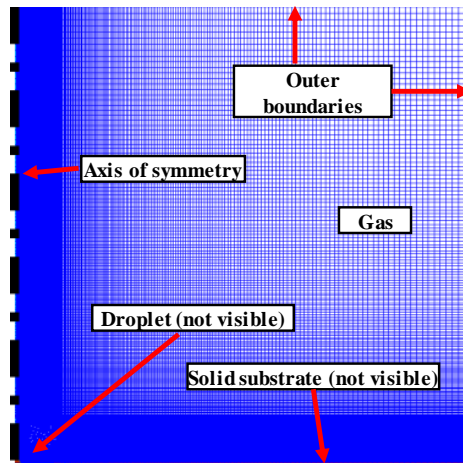
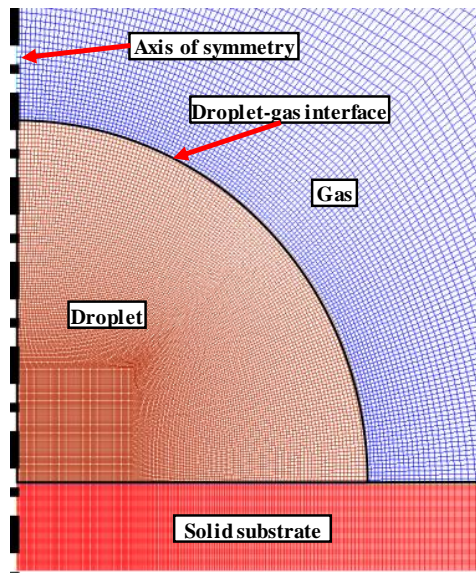


**Figure 2.** Schematic diagram of the experimental facility used for droplet freezing characterization (not to scale).

Note for the editor: 1.5 column figure



(a)



(b)

**Figure 3.** Key phases, interfaces, and boundaries of the numerical simulation domain used for the simulation of the solidification of the 10.1  $\mu\text{L}$  droplet (with mesh overlay), with views of (a) the full domain and (b) a zoomed view to reveal the details near the droplet resting on the substrate.

Note for the editor: Single column figure

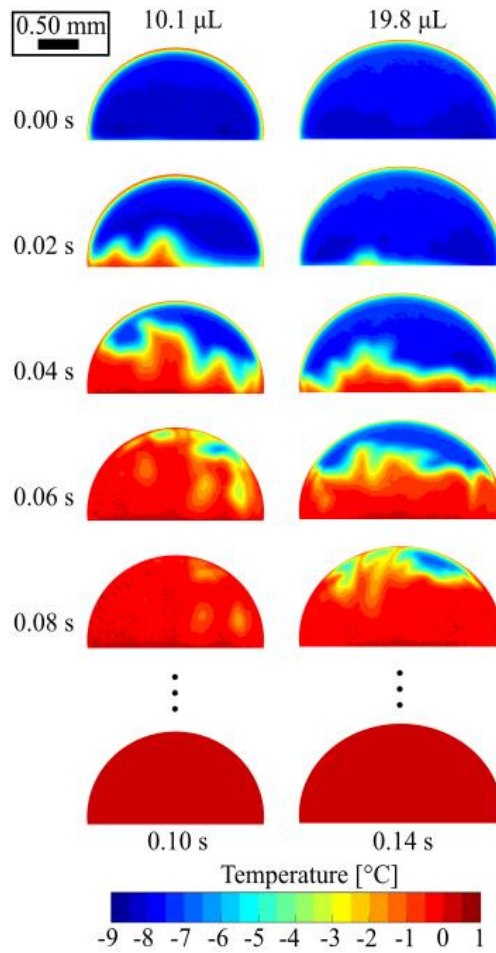


**Figure 4.** Sequence of measured side-view infrared temperature distributions on the surface 10.1  $\mu\text{L}$  (left) and 19.8  $\mu\text{L}$  (right) droplets undergoing recalescence, with the field of views cropped to the droplet to remove the immaterial background data.

Note for the editor: Single column figure

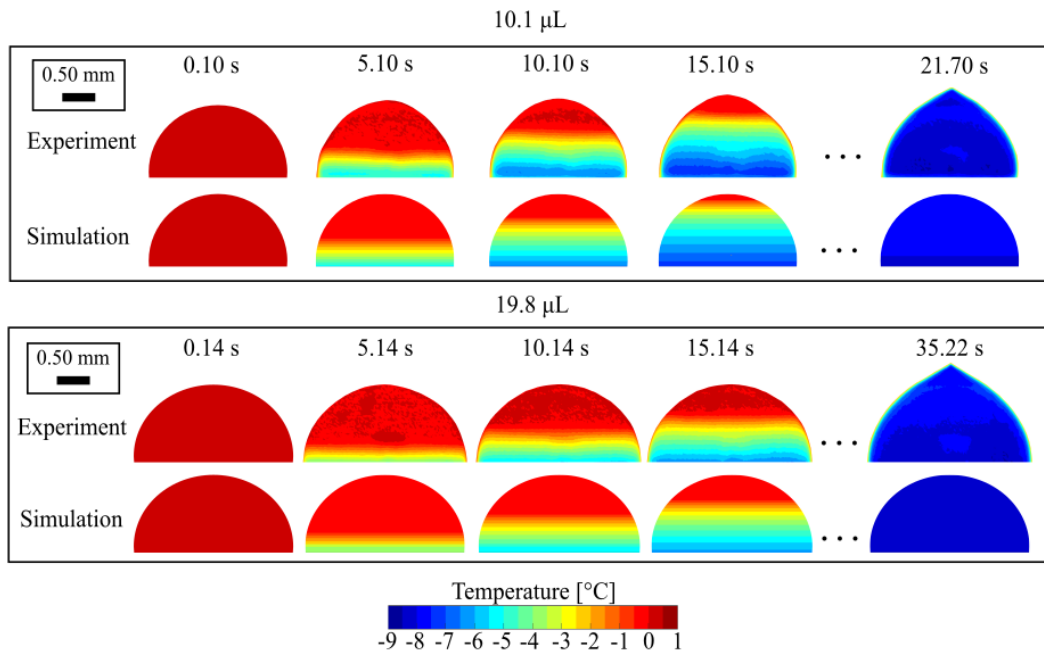
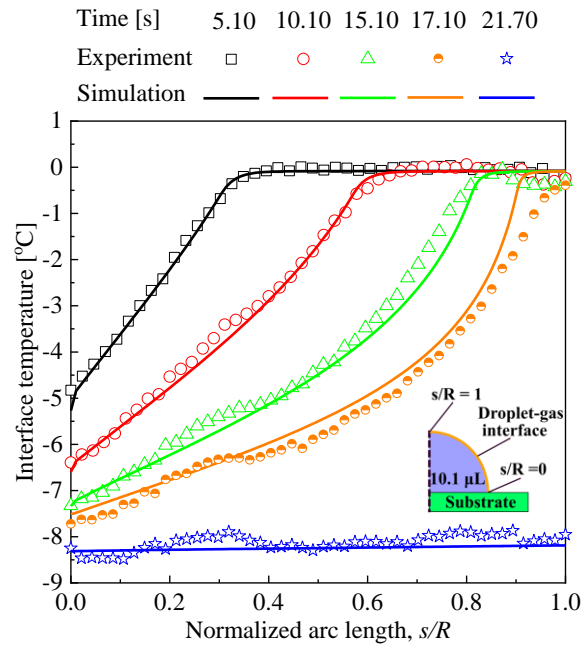


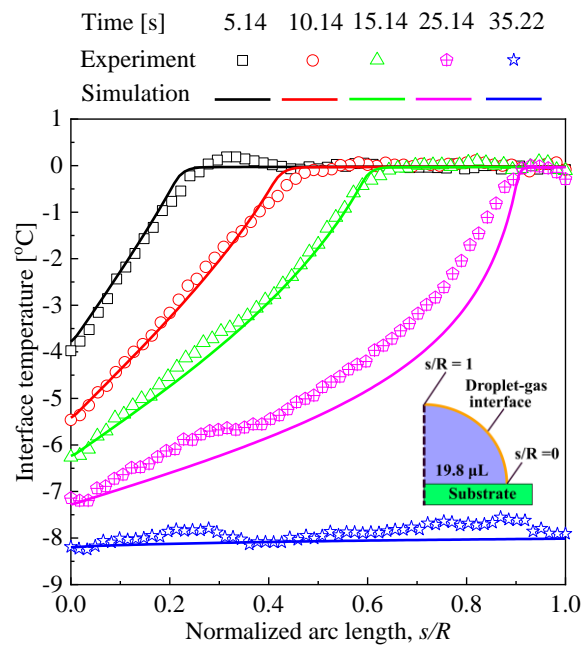
**Figure 5.** Time sequence of the surface temperature maps for 10.1  $\mu\text{L}$  and 19.8  $\mu\text{L}$  droplets during solidification after recalescence. The experimental images are obtained from the IR thermography measurements and the simulation images are generated by revolving the predicted temperature at the droplet interface around the axis of symmetry.

Note for the editor: 1.5 column figure





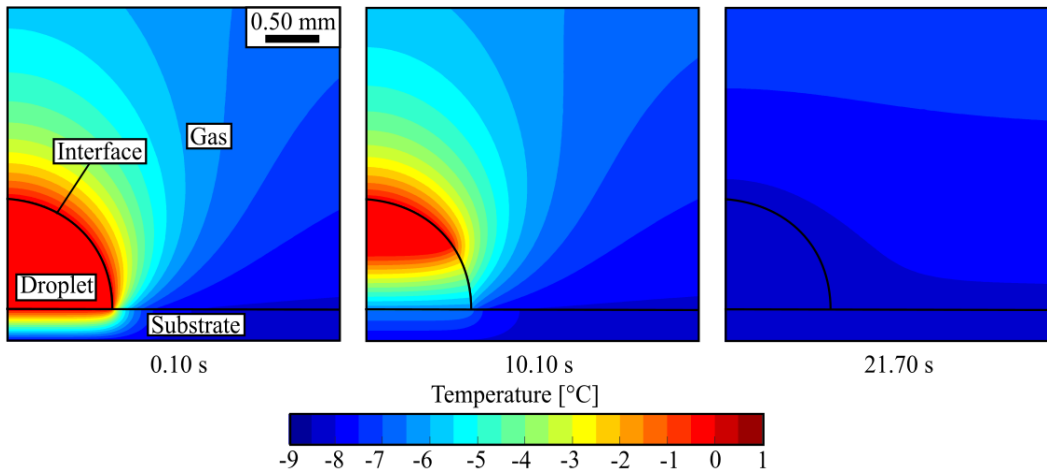
(a)



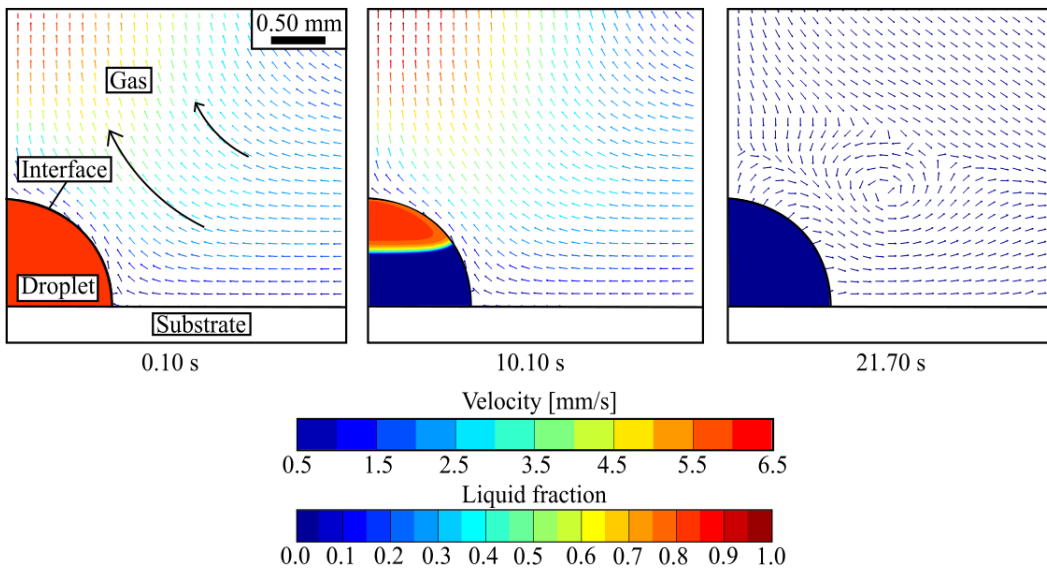
(b)

**Figure 6.** Temperature profiles along the droplet interfaces for (a) 10.1  $\mu\text{L}$  and (b) 19.8  $\mu\text{L}$  droplets at multiple different times throughout solidification after recalescence. Infrared thermography experiments (symbols) are compared to the numerical simulations (solid lines). The location along the arc of the interface ( $s$ ) is normalized by the droplet radius ( $R$ ).

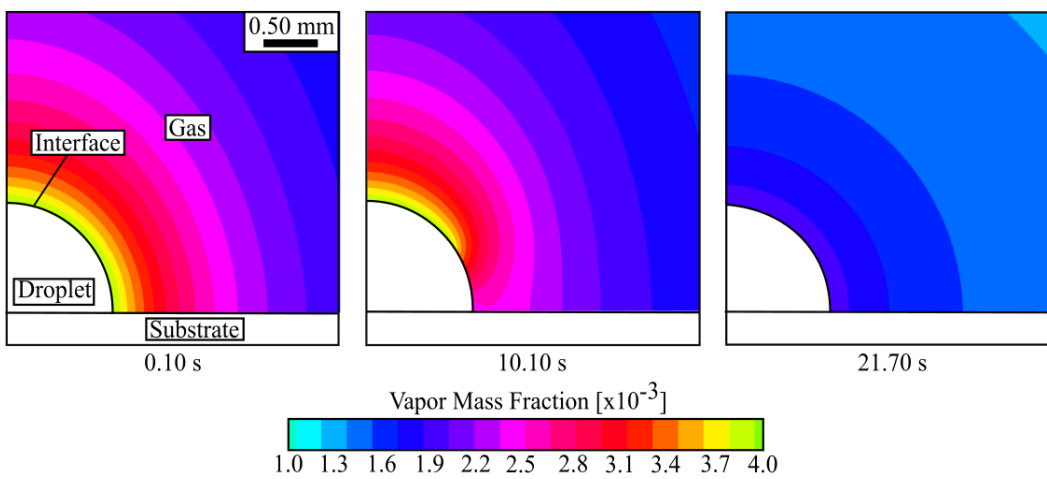
Note for the editor: Single column figure



(a)



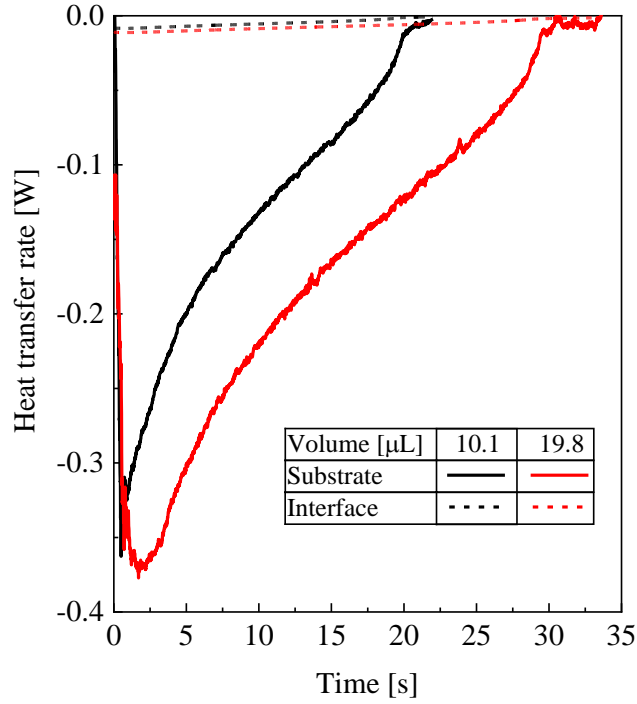
(b)



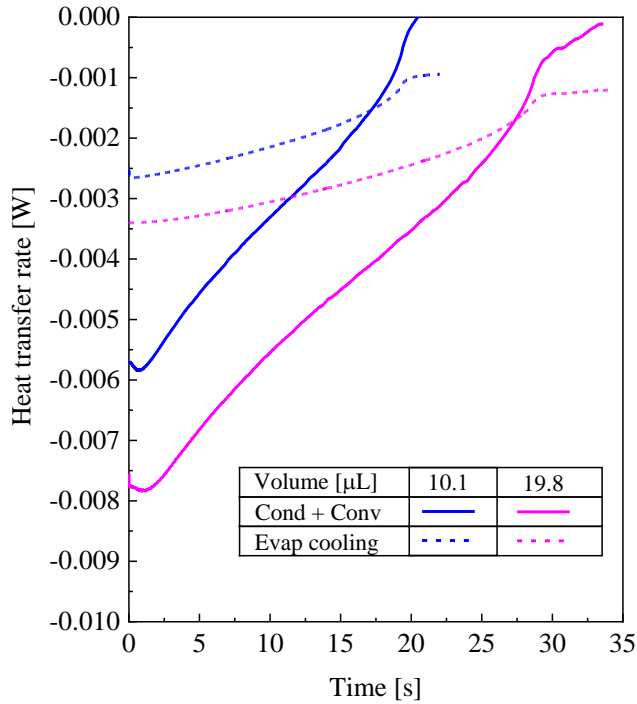
(c)

**Figure 7.** Time sequence of (a) temperature contour plots, (b) liquid fraction contour plots (within the droplet) and velocity field (in the gas domain), and (c) mass vapor fraction contour plots (in the gas domain) from the numerical simulations for the 10.1  $\mu\text{L}$  droplet.

Note for the editor: 1.5 column figure



(a)



(b)

**Figure 8.** Heat transfer rate across (a) the contact area of the droplet (solid lines) and the the droplet-gas interface (dashed lines). (b) Heat transfer rate across the droplet-gas interface via diffusion (solid lines) and natural convection (dashed lines) integrated over the droplet-gas interface and during solidification of a 10.1  $\mu\text{L}$  and a 19.8  $\mu\text{L}$  droplet.

Note for the editor: Single column figure

## Tables

**Table 1.** Thermophysical properties used in the simulations.

<b>Properties</b>	<b>Water</b>	<b>Ice</b>	<b>Gas</b>	<b>Substrate</b>
density, $\rho$ (kg/m <sup>3</sup> )	999.8 at 0.1 °C	917.5 at -5 °C	1.298 at -1.5 °C	2329
thermal conductivity, $k$ (W/mK)	0.58	2.25	0.0242	148
thermal capacity, $c_p$ (J/kg K)	4191	2027	1006.43	711.61

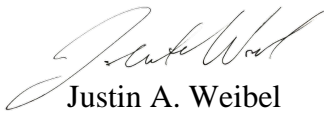
We wish to confirm that there are no known conflicts of interest associated with this publication and there has been no significant financial support for this work that could have influenced its outcome.

We confirm that the manuscript has been read and approved by all named authors and that there are no other persons who satisfied the criteria for authorship but are not listed. We further confirm that the order of authors listed in the manuscript has been approved by all of us.

We confirm that we have given due consideration to the protection of intellectual property associated with this work and that there are no impediments to publication, including the timing of publication, with respect to intellectual property. In so doing we confirm that we have followed the regulations of our institutions concerning intellectual property.

We understand that the Corresponding Author is the sole contact for the Editorial process (including Editorial Manager and direct communications with the office). He/she is responsible for communicating with the other authors about progress, submissions of revisions and final approval of proofs. We confirm that we have provided a current, correct email address which is accessible by the Corresponding Author and which has been configured to accept email from [jaweibel@purdue.edu](mailto:jaweibel@purdue.edu).

Signed by the corresponding author as follows:

  
Justin A. Weibel

# Quantifying the Pathways of Latent Heat Dissipation during Droplet Freezing on Cooled Substrates

Julian E. Castillo<sup>1</sup>, Yanbo Huang<sup>2</sup>, Zhenhai Pan<sup>2</sup>, and Justin A. Weibel<sup>1,\*</sup>

<sup>1</sup>School of Mechanical Engineering, Purdue University, West Lafayette IN 47907 USA.

<sup>2</sup>School of Mechanical Engineering, Shanghai Jiao Tong University, Shanghai, China.

\* Corresponding author.

E-mail addresses: [castil19@purdue.edu](mailto:castil19@purdue.edu) (Julian E. Castillo), [hyb728@sjtu.edu.cn](mailto:hyb728@sjtu.edu.cn) (Yanbo Huang) [panzh@sjtu.edu.cn](mailto:panzh@sjtu.edu.cn) (Zhenhai Pan), and [jaweibel@purdue.edu](mailto:jaweibel@purdue.edu) (Justin A. Weibel)

## Author Statement

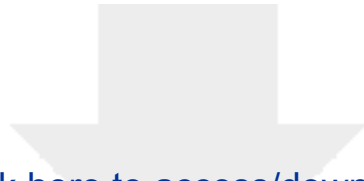
Julian E. Castillo: Conceptualization; Methodology; Validation; Investigation; Writing - Original Draft; Visualization;

Yanbo Huang: Methodology; Software; Investigation; Writing - Original Draft

Zhenhai Pan: Methodology; Software;

Justin A. Weibel: Conceptualization; Methodology; Writing - Review & Editing; Supervision





[Click here to access/download](#)

**Supplementary Material**

[SI\\_Castillo\\_Weibel\\_IJHMT\\_Aug2020.pdf](#)

